JOURNAL OF SOLID STATE CHEMISTRY 120, 80–89 (1995)

Tetrahedral Clusters of $GaMo_4S_8$-Type Compounds: A Metal Bonding Analysis

A. Le Beuze, H. Loirat, M. C. Zerrouki, and R. Lissillour

Laboratoire de Chimie du Solide et Inorganique Moléculaire, LCSIM, U.R.A. C.N.R.S. 1495, Université de Rennes I, Avenue du Général Leclerc, 35042 Rennes Cedex, France

Received November 2, 1994; in revised form June 28, 1995; accepted June 29, 1995

Extended Hückel tight binding calculations have been performed on ligated as well as on ligand-free Mo_4 and Mo_6 extended frames, in order to analyze the metal–metal bonding within the clusters and particularly the appreciable changes of the metal–metal bond lengths through the M_4 tetrahedral units contained in GaM_4X_8 (M = Mo, Nb, V, Ta; X = S, Se, Te), $Mo_4S_4Y_4$ (Y = Cl, Br, I). A comparison with the M_6 octahedral units of the MMo_6X_8 (M = Pb, Ag, La; X = S, Se) series is made. By means of DOS, COOP curves, and overlap populations, results clearly display the strong reorganization of the electronic structure of the bare metal clusters network while the ligand interactions occur, inducing a strong reduction of the strength of the metal–metal bonds. We outline the relationship between the metal–metal bond lengths and various parameters such as the valence electron count (VEC) per cluster and the nature of the ligands. Our results indicate that the two series M_4 and M_6 differ: M–M bond lengths are unaffected by the VEC in the regular M_4 cluster, whereas some M–M bond lengths undergo a significant change when the VEC increases in the distorded M_6 clusters. Likewise, it is worthy to note that metal d orbitals have a more significant effect in M_4 cluster series. In contrast, the metal–ligand covalency induces similar elongations of metal–metal bonds in the two series. © 1995 Academic Press, Inc.

1. INTRODUCTION

The solid state chemistry of Va and VIa transition metals in their low oxidation states often leads to compounds containing metal clusters of various symmetries and nuclearities. A conspicuous example is given by molybdenum in its Mo(II) oxidation state, which leads to numerous compounds containing more or less distorded octahedral Mo_6 clusters. On the other hand, the chemistry of molybdenum in its Mo(III) oxidation state has provided very few examples of compounds which exhibit delocalized metal–metal bonds in pseudo-isolated clusters analogous to the Mo_6 ones. Among them, the two series of molybdenum compounds MMo_4X_8 (M = Ga, Al, ... ; X = S, Se, ...) (1, 2) and $Mo_4S_4Y_4$ (Y = Cl, Br, I) (1c), which display tetrahedral Mo_4 clusters, have been studied. Particular attention has been devoted to their specific magnetic properties (3–5). Likewise, in ternary chalcogenide MMo_6X_8 (M = Pb, Ag, La) (6, 7) series which display Mo_6 octahedral clusters, physical properties, particularly superconductivity and magnetism, have been extensively studied (7–14). Although some theoretical studies on the metal bonding in Mo_6X_8 clusters have been reported (15), no similar studies have been made so far for the Mo_4X_4 ones. Comparison of the metal bonding between the two series has been undertaken. Following a recent study (16) on the formation of the tetrahedral clusters in the $GaMo_4X_8$ series showing that the clustering is related to a multidimensional Peierls distortion (17), we analyze in this paper the metal bonding in $GaMo_4S_8$-type compounds with the aid of EHTB calculations (see the Appendix). A comparison with that of $M'M_6X_8$ compounds is made.

The two series of compounds are analogous in terms of clusters embedded in a ligand matrix. Nevertheless, the metal–metal bond lengths may vary differently. The MMe_4X_8 (M = Ga, Al, ... ; Me = Mo Nb, V, Ta; X = S, Se, Te) compounds present a lacunar spinel-type structure AB_2X_4, the unit cell of which is shown in Fig. 1a. In this figure we discern tetrahedra (T2 = (MX_4)) and cubes (C1 = (Me_4X_4)). They are arranged in such a way that the cubes (C2 = (Me_4X_4)) become apparent at the center of the cell. The arrangement of these cells in the space reveals another type of tetrahedra (T1 = $[\,]X_4$) between two neighboring cells. Thus, the compound can be described along the threefold rotation [111] axis as the sequence of tetrahedra and cubes (Fig. 1b) T1, T2, C2, C1, T1, ... Contrary to the standard spinel structure, the Me atoms of the C1 cubes shift toward the cube center creating a Me_4 regular tetrahedral cluster with short metal–metal bond lengths (2.8 to 2.9 Å), and the Me atoms of the C2 cubes shift toward the cube outside, leading to the metal–metal distances of about 4 Å, which is too long to be considered as bonds. The top of the Table 1 summarizes the various

0022-4596/95 $12.00

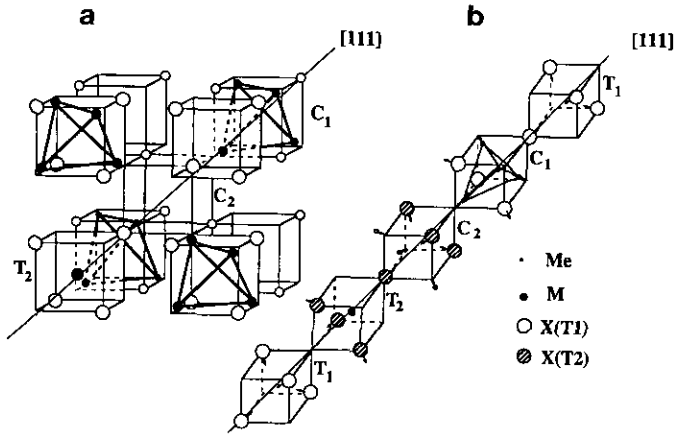

FIG. 1. Crystal structure of the MMe_4X_8-type compounds containing tetrahedral Me_4 clusters: (a) unit cell; (b) schematic description along the threefold rotation axis.

TABLE 1

Experimental Metal–Metal Distances in the $GaMo_4X_8$-Type Compounds Containing Tetrahedral Clusters and in the Ternary Chalchogenide Compounds MMo_6X_8 Containing Octahedral Clusters; Comparison Is Made with Distances in Metal Elements

		Compounds			
		$GaMo_4X_8$	$GaNb_4X_8$	GaV_4X_8	$GaTa_4X_8$
Shortest metal–metal distance (C_1 cube)	X = S	2.823	2.971	2.898	
	X = Se	2.892	3.026		3.005
	X = Te	2.915			
Metal–metal distance in metal elements		Mo–Mo 2.724	Nb–Nb 2.858	V–V 2.642	Ta–Ta 2.860
		Mo_6X_8	$AgMo_6X_8$	$PbMo_6X_8$	$LaMo_6X_8$
d_1 (Mo–Mo)$_\nabla$	X = S	2.698	2.706	2.679	2.667
	X = Se	2.694	2.701	2.697	2.682
d_2 Mo$_\nabla$–Mo$_\nabla$	X = S	2.862	2.804	2.732	2.707
	X = Se	2.827	2.776	2.734	2.725
d_3 (Mo–Mo)$_{inter}$	X = S	3.084	3.154	3.262	3.238
	X = Se	3.273	3.378	3.490	3.446

metal–metal (Me–Me) distances in some characteristic compounds.

The $PbMo_6X_8$-type ternary molybdenum chalcogenide compounds, known as the Chevrel phases, contain distorted molybdenum octahedra embedded in chalcogenide cubes (Mo_6X_8 entities), inserted in M metal cubes (Fig. 2a). The Mo_6S_8 entities of D_{3d} symmetry are slightly squeezed along the threefold rotation axis. Thus the Mo_6S_8 entities may be regarded as the superposition of two triangular planar fragments $Mo_3S_3(\nabla)$ capped by two sulfur atoms (Fig. 2b). Two intracluster metal–metal bond lengths are measured: d_1(Mo–Mo)$_\nabla$ corresponding to the bonds within Mo_3S_3 fragments and d_2 (Mo$_\nabla$–Mo$_\nabla$) corresponding to the bonds between two Mo_3S_3 fragments. Moreover, the distance between two Mo_6 clusters, d_3 (Mo–Mo)$_{inter}$, is short. In Table 1 are listed the Mo–Mo separations in four compounds: Mo_6X_8, $AgMo_6X_8$, $PbMo_6X_8$, and $LaMo_6X_8$ (X = S, Se).

As we can see in Table 1, in these two series of compounds, the intra- and interclusters Mo–Mo bond distances vary noticeably according to the nature of ligands attached to the metal clusters. Thus, the aim of the present work is to provide a better understanding of the ligand effects on the electronic structure of these metal clusters with the aid of band structure calculations performed for the bare Mo_4 and Mo_6 extended frameworks and the corresponding ligated networks $[Mo_4S_8]^{n-}$ and $[Mo_6S_8]^{n-}$. Particularly, the strength of the metal–metal bonds is analyzed with respect to the electronic effects of the valence electrons counts (VEC) and the nature of the metal and ligand atoms. The

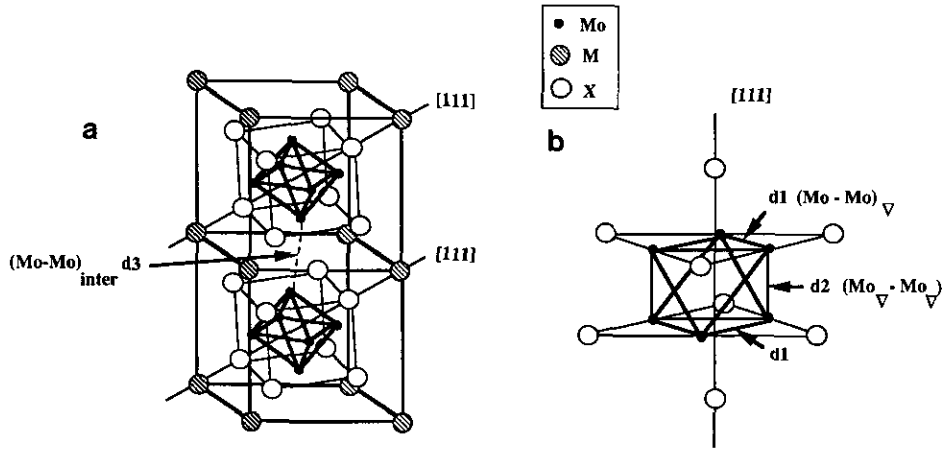

FIG. 2. Crystal structure of the MMo_6X_8 compounds containing octahedral Mo_6 clusters: (a) arrangement of Mo_6X_8 entities; (b) schematic description of the Mo_6X_8 entity along the threefold rotation axis.

calculations are carried out by means of the extended Hückel method, with the tight-binding approximation (18). The atomic parameters used are provided in the Appendix.

2. RESULTS AND DISCUSSION

Bare Metal Extended Frameworks

In order to get a comprehensive view of the ligand effects on the metal–metal bonds in the compounds of the series, we first analyze the electronic structure and metal bonding of the free-ligand metal clusters. Band structure calculations have been first performed on the metallic networks Mo_4 of $GaMo_4S_8$. The projected density of states (PDOS) and crystal-orbital-overlap-population (COOP) (18d) curves are represented for the Mo_4 and Mo_6 extended structures in Fig. 3.

This figure shows clearly large $5s$–$5s$ and $4d$–$4d$ contributions to the metal bonding. For the Mo_4 tetrahedra the whole set of orbitals spread over a 3 eV energy range and can be easily divided, from COOP curves, between bonding and antibonding bands, separated by a slight energy gap. Obviously, all the $4d$ orbitals participate homogeneously to the metal–metal bonds. In the bonding bands $5s$ metal orbitals mix largely with $4d$ ones. However, it is worthy to mention that the $5s$–$5s$ bonding interactions occur at the top of the bonding part. Thus, if bonding bands are filled up to around -11 eV, the electron count (VEC/$Mo_4 \approx 21$ e^-), according to the integration curves of partial DOS, corresponds nearly to a $4d^{4.5}\ 5s^{0.6}\ 5p^{0.1}$ Mo configuration. This yields a maximized metal–metal bonding according to the overlap population of $0.51e^-$/Mo–Mo bond. Reducing the electron count to that of $GaMo_4S_8$ (VEC/Mo_4 = 11 e^-) leads to the Mo configuration $4d^{2.5}\ 5s^{0.2}$ with always a large overlap population of 0.326 e^-/Mo–Mo bond. For such a count, ε_F lies at -11.70 eV.

The results of the bare Mo_6 frameworks are similar, although a significant increase in $5s$ contribution $4d^3\ 5s^{0.5}$ is noted for the VEC of $PbMo_6S_8$ ($22e^-$/Mo_6). This metal configuration induces strong d_1 and d_2 bonds within the distorted Mo_6 clusters according to the calculated overlap populations of $0.43e^-$/Mo–Mo and $0.39e^-$/Mo–Mo, respectively.

$GaMo_4S_8$ and $PbMo_6S_8$

Band structure calculations have been performed for the experimental structures of the two compounds. To a first approximation, the interaction between the Mo/S clusters and the cations Ga^{3+} and Pb^{2+} may be assumed to be purely ionic. Thus the Ga^{3+} and Pb^{2+} cations were not included in the calculations. The projected density of states and crystal-orbital-overlap-population plots for the $[Mo_4S_8]^{3-}$ and $[Mo_6S_8]^{2-}$ extended structures are shown in Figs. 4 and 5.

We note for the two compounds significant changes in the DOS (with respect to that of Fig. 3), which reveals a large electronic redistribution in the metal clusters. The Mo character spreads now over 10 eV but the $4d$ Mo bands concern essentially the middle and the upper part of the energy range. In fact, all bands can be separated into three parts: (i) the low-lying bands below -12.5 eV which are associated with a metal–ligand bonding character (m–L) (the capital letter means the major contribution) resulting from in-phase metal–ligand interactions; (ii) the central bands showing the strongest metal character which are mainly responsible for the formation of the metal–metal bonds. An energy gap ΔE of 1 eV separates the bonding metal–metal (M–M) bands from the antibonding (M–M^*) ones; (iii) the upper bands above -8 eV present also a strong metallic character. They represent metal–ligand antibonding (M–l^*).

After this description, it is of interest to analyze the driving forces generating those spectacular changes. Obviously they originate from strong metal–ligand interactions but these have several effects that we would like to look at in detail. Let us first go back to the crystalline structures of the tetrahedra metal clusters compounds. Figure 6 shows the ABC-type stacking of layers. The metal atoms partially occupy the octahedral sites with the following sequence: $(A_{\gamma 3/4}B_{\alpha 1/4}X_{\beta 3/4}A_{\gamma 1/4}B_{\alpha 3/4}X_{\beta 1/4}\ \ldots)$. This occupancy allows us to display the trans-edge-sharing $[MX_4]^{1}_{\infty}$ octahedra chains. Because of these octahedral sites the metal atomic orbitals are divided in the classical "t_{2g}" and "e_g" degeneracy, so we shall refer to that distinction through out the discussion below.

According to the integration curves of the partial DOS in Fig. 4, the $5s$ contribution has essentially disappeared in the energy range of the $4d$ bands, with respect to Fig. 3. The $5s$ metal orbitals are now essentially present in the low-lying ligand–metal (m–L) bonding bands (part (i)). Inversely, the $5p$ metal orbitals contribution has increased but is also located in the ligand–metal (m–L) bonding bands. It turns out, this results from the destabilization of the $5s$ orbitals with the $3p$ orbitals ligand interactions allowing then a better $5s$–$5p$ hybridization which contributes mainly to the ligand–metal bonds. Identically, the $4d$ metal orbitals participate in the low-lying (m–L) bonding bands (part (i)) but, as seen in Fig. 7, these interactions differ according to their nodal properties (i.e., e_g versus t_{2g} orbitals for the tetrahedral clusters). The metal e_g orbitals are now mainly involved in the ligand–metal (m–L) bonding bands (part (i)). In return, this leads to a dominant e_g metallic character in the metal–ligand (M–l^*) antibonding upper bands counterpart (part (iii)). The $4d$ t_{2g} orbitals are mainly the only ones involved in the central metal–metal bonding (part (ii)). According to the T_d symmetry of the

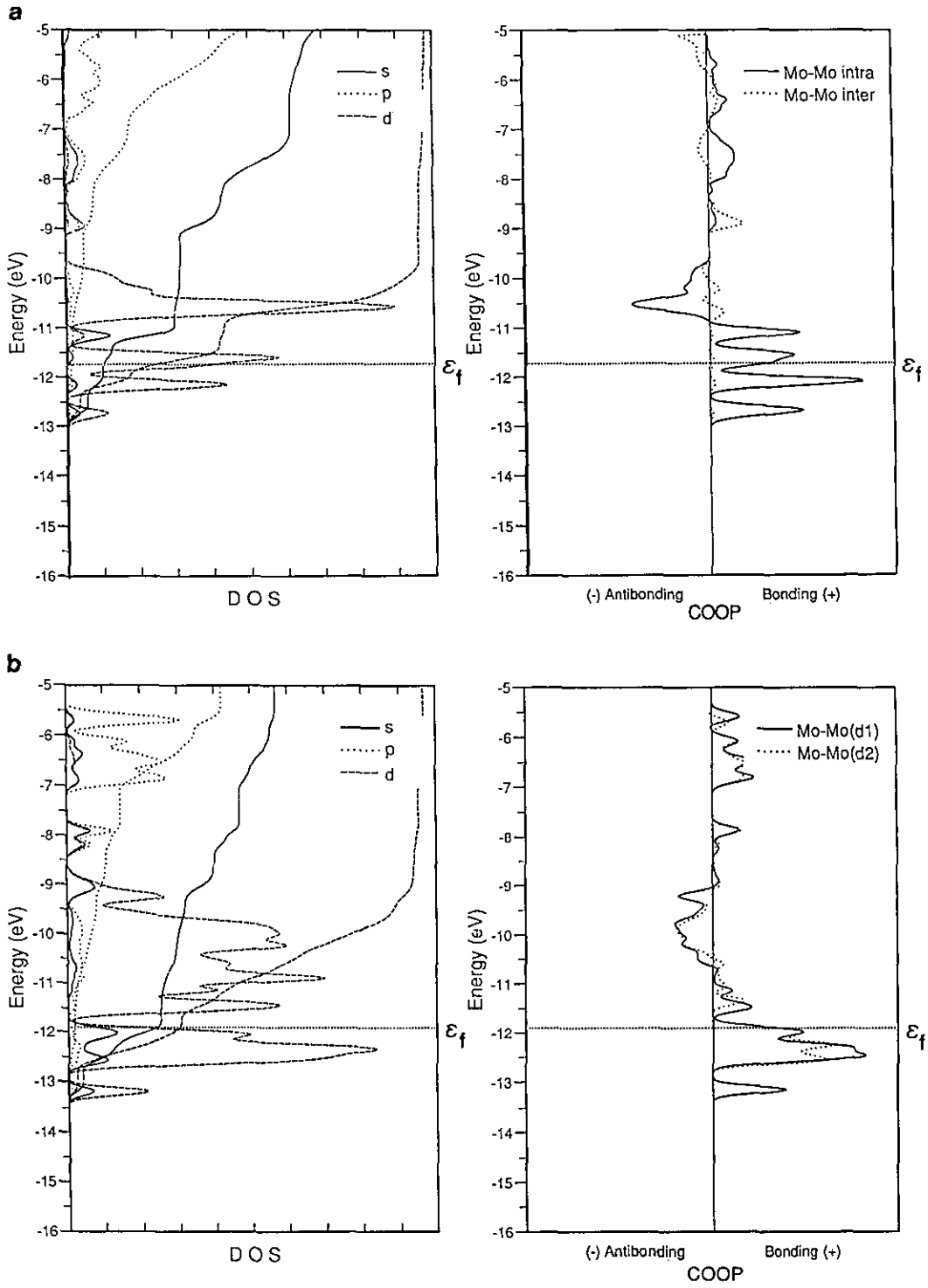

FIG. 3. Calculated results for the metallic free-ligated networks (a) $[Mo_4]$, (b) $[Mo_6]$ of the crystal structures of $GaMo_4S_8$ and of $PbMo_6S_8$: plots of the projected DOS on the *s*, *p*, and *d* metal orbitals and their corresponding integrated curves (distinguished by their continual growing through the valence band), and of the COOP curves for metal–metal bonds. The Fermi level in the two series is calculated with the same metal electron count as that in the corresponding ligated compounds.

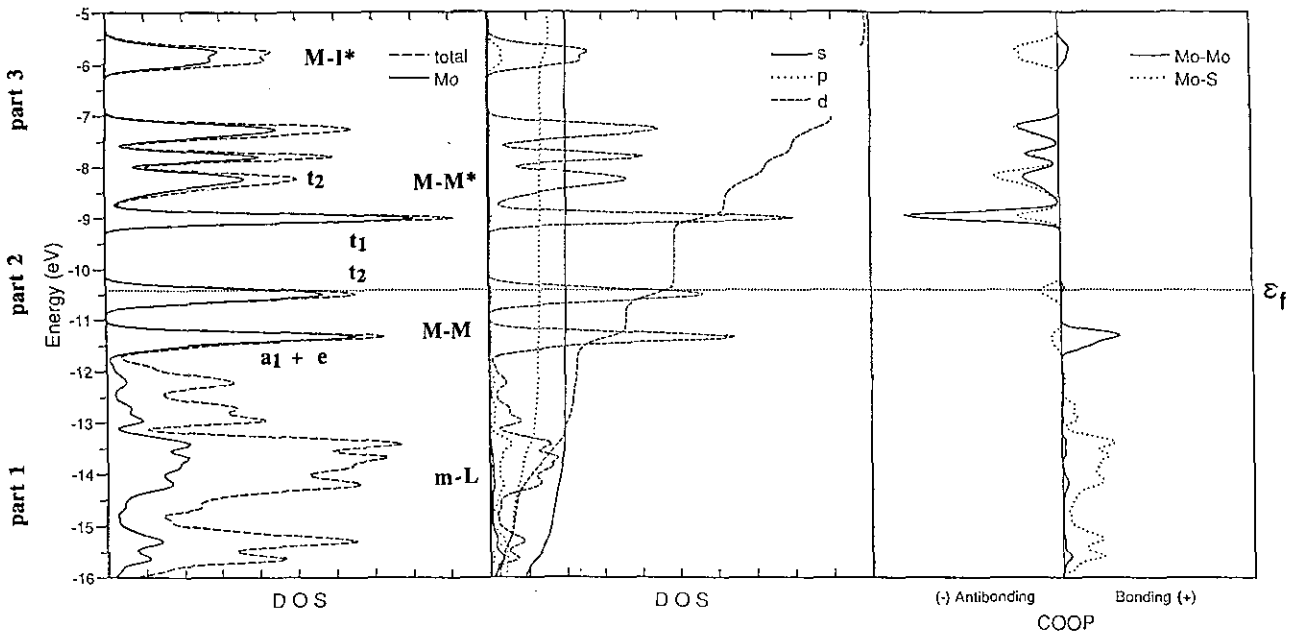

FIG. 4. Theoretical results (projected DOS and COOP curves) for the $[Mo_4S_8]^{3-}$ network corresponding to the $GaMo_4S_8$ compound.

extended structure, the bonding (M–M) bands are of a_1 and e symmetries while the $1t_2$ band is rather nonbonding. The antibonding (M–M^*) bands are of t_1 and t_2 symmetries.

Addition of the ligand shell leads to large changes in the electronic configuration of the metal atoms. In the Mo_4 series, for a formal VEC of $11e^-/Mo_4$, which puts the Fermi level at -10.72 eV, the metal configuration is $4d^{4.67}$ $(t_{2g}^{3.36}\, e_g^{1.30})5s^{0.40}\, 5p^{0.76}$. For a formal VEC of $0\, e^-/Mo_4$, which puts the Fermi level near -12.5 eV, the metal configuration is $4d^{2.33}(t_{2g}^{1.03}\, e_g^{1.30})5s^{0.4}\ 5\ p^{0.72}$. This reflects a strong covalency between the metal atoms and the ligands. A rather strong *spd* hybridyzation of the metal orbitals occurs which consequently enhances the metal–metal bonding. The $5s$ and $4d$ e_g orbitals are involved essentially in metal–ligand

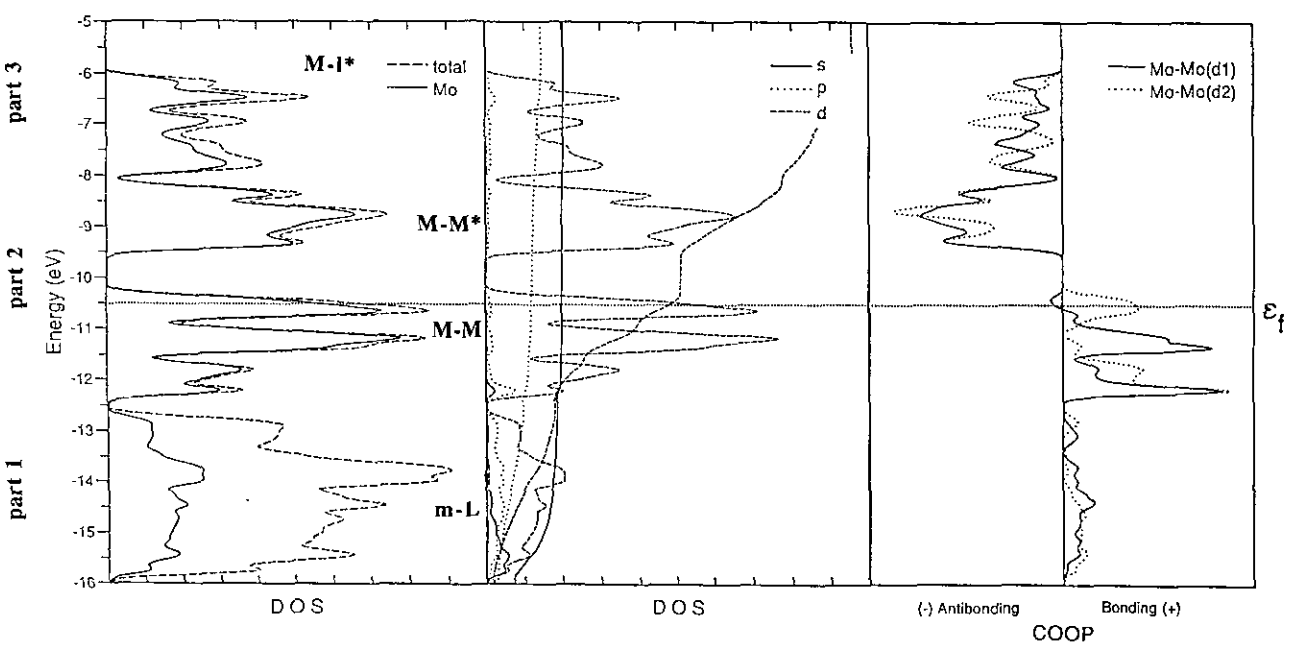

FIG. 5. Theoretical results (projected DOS and COOP curves) for the $[Mo_6S_8]^{2-}$ network corresponding to the $PbMo_6S_8$ compound.

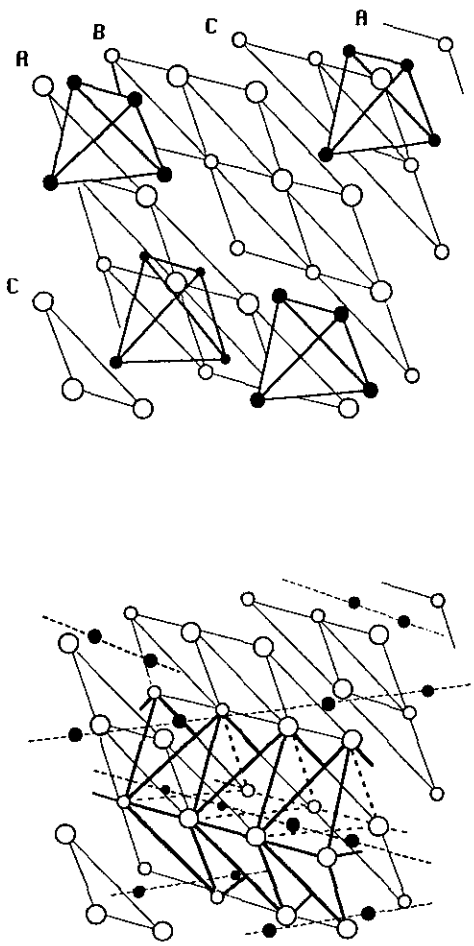

FIG. 6. View of the crystal structure of $GaMo_4S_8$ displaying the tetrahedral clusters within the ABC-type stack of the anion layers and the octahedral sites of the metals.

bonds; only the $4d$ $t_{2g}^{2.3}$ electrons are available to make the metal–metal bonding (*M–M*, part (*ii*)). This induces, according to the overlap populations, a significant decrease in the strength of the metal–metal bonds (0.150 e^-/Mo–Mo, with a VEC of 11 e^-/Mo_4). As seen in Figs. 4 and 5, similar metal–ligand bonding covalency is noticed with similar effects on the metal bonding within the clusters for the two series of compounds. For the octahedral Mo_6 clusters, at the Fermi level with a formal VEC of 22 e^-/Mo_6, the metal configurations is $4d^{5.12}5s^{0.40}$ $5p^{0.72}$. While for a formal VEC of 0 e^-/Mo_6, which puts the Fermi level near −12.5 eV, the metal configuration is $4d^{1.7}$ $5s^{0.36}$ $5p^{0.6}$. In this case, there are more $4d$ electrons ($4d^{3.4}$) and a weak participation of $5s$ and $5p$ electrons ($5s^{0.04}5p^{0.12}$) to form the metal–metal bonds, which leads to larger overlap populations for the two bonds d_1 and d_2 (0.242 e^- and 0.221 e^-/Mo–Mo, respectively) in the Mo_6 cluster.

The comparison of the COOP curves of Figs. 4 and 5 with those of the bare clusters displayed in Fig. 3 also provides a better comprehensive view of the metal bonding. In the two series, we note a displacement of the metal–metal bonding character in the ligand energy range, reflecting the metal–ligand covalency discussed above. For the ligated tetrahedral clusters, the metal–metal bonding is essentially found in the lower part of the $4d$ bands ($1a_1$ and $1e$) while at the Fermi level the $4d$ band ($1t_2$ symmetry) is nonbonding. Concerning the octahedral series, the three metal–metal bonds of the extended structure display, at the Fermi level, various bonding characters: while the $(Mo–Mo)_\nabla(d_1)$ is slightly antibonding, the Mo_∇–Mo_∇ (d_2) contact is strongly bonding, and the $(Mo–Mo)_{inter}$ (d_3) band is strongly antibonding, on the other hand.

Influence of the Nature of the Ligands

The substitutions of S by Se then Te in these compounds do not modify the number of the valence electrons of the metallic cluster but increase the metal–ligand covalency. As the ligand *L* bands go up, the ligand contribution to the (*m–L*) bands decreases and simultaneously the metal–metal bonding and antibonding contributions in those bands increase. Conversely, in the *M–M* bands, the ligand contribution increases and the metal–metal bonding contribution simultaneously decreases.

To examine the effect of different *X* (S, Se, T) within the MMe_4X_8 series, we have performed band structure calculations on the experimental structure of $GaMo_4S_8$, with a VEC of 11 electrons, by only varying the ligand H_{ii} parameters. The overlap populations of the metal–metal bonds decrease from 0.151 to 0.129 then to 0.099 with sulfur, selenium, and tellurium parameters, respectively. Analogous changes are obtained with calculations on the experimental geometry of $GaMo_4Se_8$ and $GaMo_4Se_4Te_4$. These computed values agree with the observed metal–metal bond elongations from S to Te (see Table 1). They can quantitatively be interpreted from the metal electron configurations calculated at the Fermi level: $GaMo_4Se_8$—$5s^{0.40}5p^{0.84}$ $4d^{5.15}(t_{2g}^{3.57}$ $e_g^{1.58})$; $GaMo_4Se_4Te_4$—$5s^{0.38}$ $5p^{0.87}$ $4d^{5.83}(t_{2g}^{3.87}$ $e_g^{1.93})$, and for the formal metal d^0 configuration: $GaMo_4Se_8$—$5s^{0.39}$ $5p^{0.80}$ $4d^{3.14}(t_{2g}^{1.63}$ $e_g^{1.49})$; $GaMo_4Se_4Te_4$—$5s^{0.37}$ $5p^{0.81}$ $4d^{4.02}(t_{2g}^{2.32}$ $e_g^{1.70})$. As the *M*–ligand covalency increases, the metal t_{2g} participation increases in the low-lying metal–ligand bonding part (i), which gives rise to an increase in the metal–metal overlap population at the formal $4d^0$ metal configuration ($GaMo_4S_8$: 0.065; $GaMo_4Se_8$: 0.075; $GaMo_4Se_4Te_4$: 0.110). Conversely, the t_{2g} electron count responsible for the metal–metal bonding in the energy part (ii) is reduced ($GaMo_4S_8$: $t_{2g}^{2.30}$, $GaMo_4Se_8$: $t_{2g}^{1.94}$, $GaMo_4Se_4Te_4$: $t_{2g}^{1.55}$). This electron loss leads to a large reduction of the metal–metal bonding character in the metal $4d$ bands, which counterbalances and even exceeds the increase within the metal–ligand energy part. This gives rise to the trend of the overlap population calcu-

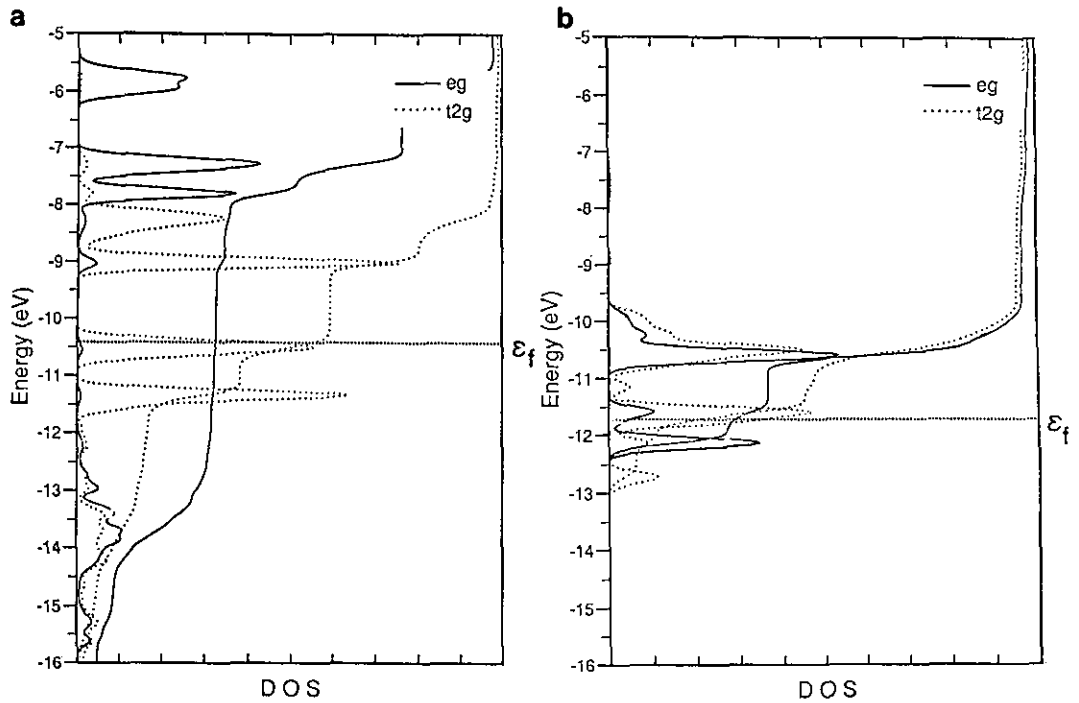

FIG. 7. Partial DOS projected on the metal "e_g" and "t_{2g}" 4*d* orbitals for: (a) $[Mo_4S_8]^{3-}$ network; (b) [Mo4] network.

lated at the Fermi level. Thus the more the ligand covalency increases, the more the metal–metal bonding decreases.

In the series containing octahedral clusters, the same trend is expected. The Mo–Mo bond overlap population calculations, performed on the experimental geometries of $M Mo_6S_8$ compounds, by varying only H_{ii}'s parameters of the ligands, show the same qualitative result (see Table 2), i.e., the tendency to increase the three metal–metal distances. Experimentally, the intercluster distance d_3 varies largely in this way, and the intracluster distances d_2 and d_1 do not vary significantly (see Fig. 8).

Influence of the Cluster Electron Count

The cluster electron number depends on both the nature of the transition metals and the ligands. In the MMe_4X_8-type compounds, the chalcogenide ligands provide in all compounds the same electron number. On the other hand, molybdenum gives 3 more electrons than niobium, tantalum, or vanadium. Thus the compounds studied here present either 7 or 11 electrons per cluster. These electrons

TABLE 2
Electron Populations Corresponding to Mo–Mo Bonds in $M Mo_6X_8$-Type Compounds

Compound:	$PbMo_6X_8$		Mo_6X_8	
X:	S	Se	S	Se
(Mo–Mo)∇ d_1	0.242	0.220	0.250	0.230
Mo∇–Mo∇ d_2	0.221	0.197	0.146	0.134
$(Mo–Mo)_{inter}$ d_3	0.061	0.053	0.108	0.099

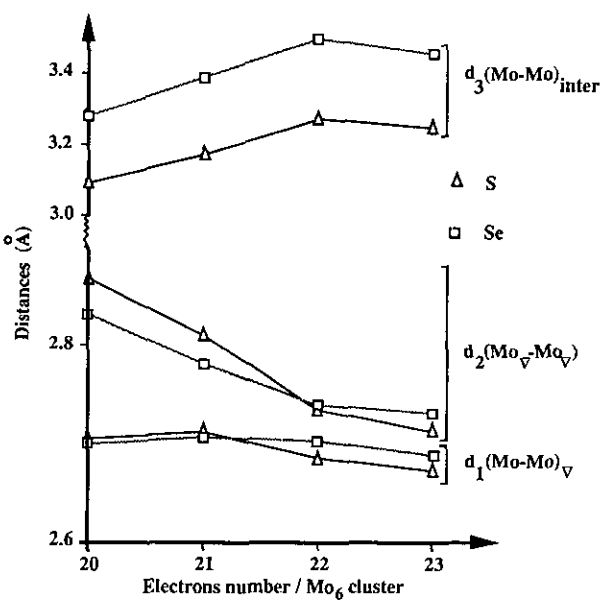

FIG. 8. Variations of experimental Mo–Mo distances with respect to the electron count in $M Mo_6X_8$-type compounds. The counts of 20, 21, 22, and 23 electrons/Mo_6 correspond, respectively, to Mo_6X_8, $AgMo_6X_8$, $PbMo_6X_8$, and $LaMo_6X_8$.

TABLE 3
Electron Overlap Populations Corresponding to Mo–Mo Bonds in $PbMo_6S_8$ as a Function of the Electron Count by Cluster

	Electrons number/cluster			
	20	21	22	23
$(Mo–Mo)^{\nabla}$ d_1	0.243	0.242	0.242	0.240
$Mo^{\nabla}–Mo^{\nabla}$ d_2	0.208	0.214	0.221	0.228
$(Mo–Mo)_{inter}$ d_3	0.071	0.067	0.061	0.054

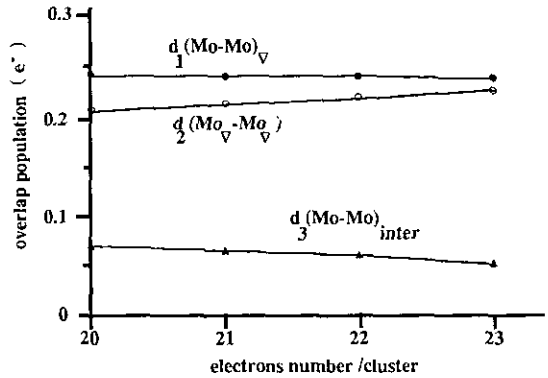

FIG. 9. Evolution of the Mo–Mo overlap population of the metal–metal bonds in $PbMo_6S_8$ with respect to the electron number by cluster.

are housed in the $1t_2 + 1a_1 + 1e$ bands. These bands would be completely filled with 12 electrons. Compounds with 7 electrons per cluster correspond to one electron in the $1t_2$ band and those with 11 electrons per cluster to a larger occupation of this band (five electrons).

As shown by the COOP curves of Fig. 4, the Mo–Mo bonding levels are almost full with 6 electrons per cluster (occupation of bands $1a_1$ and $1e$), since the absolute value of the $1t_2$ overlap population is very small. Therefore, the $1t_2$ band contributes weakly, at the Fermi level, to the stability of the tetrahedral clusters. This is quantitatively revealed by the calculations of the overlap populations related to the Mo–Mo bond in the tetrahedral clusters for 6 and 11 electrons per Mo_4 cluster: the computed overlap population varies between 0.149 and 0.152. This shows clearly that the overlap population of the metal–metal bonds is independent of the $1t_2$ band occupation in these compounds.

On the COOP curves of $PbMo_6S_8$ (see Fig. 5), the Fermi levels given for 20 and 23 electrons correspond to the minimum and maximum electron counts observed for the studied MMe_6X_8 compounds, respectively. The COOP curves show that the increase in the electron count from 20 to 23 leads to an increase in the d_1 and d_3 distances, and a decrease in the d_2 distance. The change of d_1 is small. This is clearly shown in Table 3 and Fig. 9, where the Mo–Mo bond overlap populations are represented. This agrees with the experimental results given in Fig. 8. Consequently, the electron count seems to have a more significant effect in the $M–M$ bond lengths for compounds with octahedral clusters than those with tetrahedral clusters.

Influence of the d Metal Orbital in MMe_4X_8 Compounds

The comparison of the $Me–Me$ bond lengths in $GaMe_4X_8$ compounds with those in metal elements (see Table 1) provides us with a criterion for the $Me–Me$ bond strength. First, we note that the $Me–Me$ bonds are weaker in all these compounds than in the metal element (3.5 to 9%). In the Mo, Nb, and Ta compounds, they match rather well (3.5 to 5.8%), but is weaker (9%) in the V compounds.

We carried out overlap population calculations in order to analyze and find out the important factors leading to this $M–M$ bond length variation. The metals differ in their electronegativity, electron number, and valence orbital type (3*d*, 4*d*, or 5*d*). This is also related to electronegativity and orbital diffuseness. A decrease in the metal electronegativity induces the rising of $M–I$ levels and thus a $M–M$ bonding increase (the antibonding $M–M$ bond is not occupied). Overlap population calculations carried out for the experimental geometry of $GaNb_4Se_8$ compound, by varying only the H_{ii}'s parameters of the transition metal, display a $M–M$ bond strengthening when the metal electronegativity decreases from Mo to Nb to Ta (see Table 4). In contrast, the overlap populations in the vanadium compound are much lower although its electronegativity is close to that of niobium. This is due to the fact that the 3*d* orbital is less diffuse than the 4*d* or 5*d* orbitals. This corresponds to smaller $M–M$ interactions. In this case, the orbital dif-

TABLE 4
Influence of the Nature of the Metal *Me* in the MMe_4X_8-Type Compounds

		Metal (*Me*)			
		Mo	V	Nb	Ta
Electronegativity χ (Pauling)		2.16	1.63	1.6	1.5
Electronic Population related to *Me–Me* bond	7 e^-/cluster	0.150	0.115	0.158	0.204
	11 e^-/cluster	0.151	0.120	0.152	0.177

Note. The electron overlap populations are calculated on the $GaMo_4S_8$ compound geometry with various extended Hückel parameters for *Me*.

TABLE A1
Parameters Used for Extended Hückel Calculations

Orbital		H_{ii}(eV)	ζ_1	ζ_2	C_1[a]	C_2[a]
S	3*s*	−20.00	2.12			
	3*p*	−13.30	1.83			
Se	4*s*	−20.50	2.44			
	4*p*	−13.05	2.07			
Te	5*s*	−20.50	2.57			
	5*p*	−12.90	2.16			
V	3*d*	−11.0	4.40	1.80	0.4550	0.7510
	4*s*	−8.80	1.60			
	4*p*	−5.34	1.60			
Mo	4*d*	−11.06	4.54	1.90	0.5899	0.5899
	5*s*	−8.77	1.96			
	5*p*	−5.69	1.90			
Nb	4*d*	−10.10	4.08	1.64	0.6401	0.5516
	5*s*	−8.10	1.90			
	5*p*	−4.86	1.85			
Ta	5*d*	−9.50	4.00	1.60	0.6815	0.6815
	6*s*	−7.80	2.280			
	6*p*	−4.56	2.241			

[a] Coefficients in the double ζ expansion.

fuseness prevails. The extended Hückel parameters include implicitly the electronegativity factor in the VSIP parameters and also the orbital diffuseness in the orbital exponent parameters. In Mo and Nb elements, the same orbital type 4*d* is involved, but electronegativity and valence electron number change somewhat. Since the valence electron number has no great significance, electronegativity prevails, as suggested by the overlap population calculations. Tantalum, with the lowest electronegativity and 5*d* orbitals, involves the highest overlap populations for the *M*–*M* bonds.

3. CONCLUSION

The present extended Hückel calculations allow us to show the large relaxation of the electronic structure of the bare Mo_4 cluster when they are surrounded by ligands. The 5*s* and 4*d* e_g metal orbitals are involved essentially with metal–ligand bonds. The 4*d* t_{2g} electrons remains only available for the metal–metal bonding which induces a strong reduction of the strength of the metal–metal bonds. Our results have shown the role of some factors on the *M*–*M* bond lengths in a series of compounds containing tetrahedral and octahedral metallic clusters. The importance of the ligand covalency factor is emphasized in the two series of compounds. In contrast, the *Me*–*Me* distances are controlled by the electron count in the octahedral clusters. Finally, the present study has shown that the valence shell of the *d* metal orbitals has a large influence on the *M*–*M* bond lengths in tetrahedral clusters encountered in the MMe_4X_8-type compounds.

APPENDIX

The bond distances used for the calculations were taken from the experimental structure of GaM_4X_8, $PbMo_6S_8$, and Mo_6S_8 compounds. Tight-binding computations were carried out within the extended Hückel formalism. The parameters are listed in Table A1. The DOS, the *M*–*M* bond overlap populations, and the electron configurations were calculated using a special set of *k* points of the irreductible wedge of the Brillouin zone.

ACKNOWLEDGMENT

The authors are grateful to Dr. J-F. Halet for helpful discussions and comments.

REFERENCES

1. (a) A. Balz, *Mater. Res. Bull.* **8,** 983 (1973); (b) C. Perrin, R. Chevrel, and M. Sergent, *C. R. Acad. Sci.* **230c,** 949 (1975); (c) C. Perrin, R. Chevrel, and M. Sergent, *C. R. Acad. Sci.* **281c,** 23 (1975); (d) J. M. Van Den Berg and D. Brazen, *J. Solid State Chem.* **14,** 203 (1975).
2. H. Ben Yaich, Thesis, Université de Rennes I, France, 1988.
3. (a) A. K. Rastogi, A. Berton, J. Chaussy, R. Tournier, M. Potel, R. Chevrel, and M. Sergent, *J. Low Temp. Phys.* **52,** 539 (1983); (b) A. K. Rastogi, R. Tournier, A. Berton, M. Potel, R. Chevrel, and M. Sergent, *J. Low Temp. Phys.* **55,** 551 (1984); (c) H. Ben Yaich, J. C. Jegaden, M. Potel, R. Chevrel, M. Sergent, A. Berton, J. Chaussy, A. K. Rastogi, and R. Tournier, *J. Solid State Chem.* **51,** 212 (1984); (d) S. Berretil, Thesis, Université de Paris V, France, 1987; (e) V. Shamrai, G. Leitus, *Sov. Phys. Solid State* (*Engl. Transl.*) **29**(8), 1312 (1987).
4. O. Pena, H. Ben Yaich, M. Potel, and M. Sergent, *Physica B* **163,** 435 (1990).
5. (a) M. François, K. Yvon, W. Lengauer, H. Ben Yaich, P. Gougeon, M. Potel, and M. Sergent, *Z. Kristallogr.* **196,** 111 (1991); (b) M. François, A. Alexandrox, K. Yvon, H. Ben Haich, P. Gougeon, M. Potel, and M. Sergent, *Z. Kristallogr.* **200,** 47 (1992).
6. (a) R. Chevrel, M. Sergent, and J. Prigent, *J. Solid State Chem.* **3,** 515 (1971); (b) R. Chevrel, Thesis, Université de Rennes, France, 1974.
7. R. Chevrel and M. Sergent, *in* "Superconductivity in Ternary Compounds" (O. Fischer and M. B. Maple, Eds.), Vol. 1. Springer Verlag, Berlin/Heidelberg/New York, 1982.
8. O. Pena and M. Sergent, *Prog. Solid State Chem.* **19**(3), 165 (1989).
9. R. Chevrel, P. Rabiller, S. Boudjada, L. Burel, and M. Sergent, *in* "Proceedings, International Workshop on Chevrel phasis Superconductors," p. 1. Chavannes de Bogis, Switzerland, 1991.
10. P. Svedlindh, K. Nishanen, P. Norling, P. Nordblad, L. Lungren, C. Rossel, M. Sergent, R. Chevrel, and M. Potel, *Phys. Rev., B* **43,** 1735 (1991).
11. M. Sergent, C. Perrin, S. Ihmaine, A. Perrin, H. Ben Yaich, O. Pena, R. Chevrel, P. Gougeon, and M. Potel, *J. Chim. Phys.* **88,** 2123 (1991).
12. P. Selvam, D. Cattani, J. Cors, M. Decroux, P. Niederman, S. Ritter, O. Fischer, P. Rabiller, and R. Chevrel, *J. Appl. Phys.* **72,** 4232 (1992).
13. R. Chevrel, *in* "Modern Perspectives in Inorganic Crystal Chemistry" (E. Parthe, Ed.), Nato Asi Series C, p. 17. Kluwer Academic, Dordrecht/Norwell, MA, 1992.
14. M. François, K. Yvon, D. Cattani, M. Decroux, R. Chevrel, M. Sergent, S. Boudjada, and T. Wroblewski, *J. Appl. Phys.* **75,** 423 (1994).
15. (a) L. F. Mattheis and C. Y. Fong, *Phys. Rev., B* **15,** 1760 (1977); (b) D. W. Bullet, *Phys. Rev. Lett.* **39,** 664 (1977); T. Jalborg and A. J.

Freeman, *Phys. Rev. Lett.* **44,** 178 (1980); (d) H. Noll, W. Klose, and O. K. Anderson, *in* "Superconductivity in Ternary Compounds," (O. Fischer and M. B. Maple, Eds.), Vol. 1. Springer-Verlag, Berlin/Heidelberg/New York, 1982; (e) A. Le Beuze, M. A. Makhyoun, R. Lissillour, and H. Chermette, *J. Chem. Phys.* **76,** 6060 (1982); (f) T. Hughbanks and R. Hoffmann, *J. Am. Chem. Soc.* **105,** 1150 (1983); (g) R. G. Wooley, *Inorg. Chem.* **24,** 3519 (1985).

16. A. LeBeuze, M. C. Zerrouki, H. Loirat, and R. Lissillour, *J. Alloys Compounds* **190,** 1 (1992).
17. (a) R. E. Peierls, "Quantum Theory of Solids." p. 108. Oxford Univ. Press, London, 1955; (b) M. H. Whangbo, *Acc. Chem. Res.* **16,** 35 (1983); (c) M. H. Whangbo, *in* "Crystal Structures and Properties of Materials with Quasi-One-Dimensional Structures" (J. Rouxel, Ed.), p. 35. Reidel Ordrecht, The Netherlands, 1986; (d) E. Canadel and M. H. Whangbo, *Chem. Rev.* **91,** 965 (1991).
18. (a) R. Hoffmann, *J. Chem. Phys.* **39,** 1397 (1963); (b) M. H. Whangbo and R. Hoffmann, *J. Am. Chem. Soc.* **100,** 6093 (1978); (c) M. H. Whangbo, R. Hoffmann, and R. B. Woodward, *Proc. R. Soc., London, A* **366,** 29 (1979); (d) J.-Y. Saillard and R. Hoffmann, *J. Am. Chem. Soc.* **106,** 2006 (1984).